# Current Harmonic Minimum Pulse Width Modulation for Dual Three-Phase PMSM System With 3L-NPC Inverter and Output Filter

Chuanqiang Lian, LiYuan Guo, GuanDa Xu, Fei Xiao, Ruitian Wang, Shan Gao, Jilong Liu, and Weiwei Zhang

***Abstract*—The dual three-phase permanent magnet synchronous motor (DTP-PMSM) has wide applications in fields such as wind power generation, electric vehicles, and flywheel energy storage. Reducing the current harmonics of the DTP-PMSM is beneficial for enhancing operational efficiency, diminishing noise and vibration, and improving electromagnetic compatibility, which is of significant importance for boosting the overall performance of the system. This article focuses on the current harmonic minimum pulse width modulation (CHMPWM) for the surface-mounted DTP-PMSM with a 3L-NPC inverter and an output filter. Based on the system model, the relationship between the switching angles and the harmonic current of the motor is derived, and the mathematical model of CHMPWM is established. Furthermore, the optimal switching angles that minimize the current harmonics can be obtained by solving the established optimization problem. The proposed CHMPWM takes into account the effect of filter and motor parameters on the current harmonic characteristics, which is the main difference from the conventional CHMPWM. Simulation and experimental studies were conducted on a 1 MW/40MJ flywheel energy storage system, and the results show that compared to sine PWM and space vector PWM, the current harmonics of the proposed CHMPWM are reduced by more than 40% on average. Compared to the conventional CHMPWM, the proposed CHMPWM further reduces the current harmonics by more than 20% on average and exhibits good robustness to motor parameters.**

***Index Terms*—3L-NPC inverter, current harmonic minimum pulse width modulation (CHMPWM), dual three-phase permanent magnet synchronous motor (DTP-PMSM), output filter.**

## I. Introduction

AS AN important piece of power equipment in modern industry, the performance and efficiency of motors directly affect the energy consumption and productivity of the whole society. Dual three-phase permanent magnet synchronous motor (DTP-PMSM) has the advantages of high torque density, low torque pulsation, high efficiency, and high reliability and has been widely used in the fields of wind power generation, electric vehicles, intelligent manufacturing, flywheel energy storage, rectifier power generation for ships and vehicles, and permanent magnet propulsion [1], [2], [3].

Current harmonics are one of the key indicators of the motor system, which will bring different degrees of harm to the equipment and system. Many countries and regions have clear requirements on the current harmonic content of the motor system. Strict control of current harmonics in motor systems can enhance machine efficiency, improve electromagnetic compatibility, increase control precision, reduce noise and vibration, prolong the lifespan of the machines, enhance the stability of the system, etc., which is crucial for enhancing the overall performance of the system [4], [5].

Pulse width modulation (PWM) is one of the core technologies in power electronics and directly determines the distribution of current harmonics. PWM strategies primarily include sine PWM (SPWM) [6], [7], space vector PWM (SVPWM) [8], [9], intermediate 60° modulation [10], [11], selected harmonic elimination PWM (SHEPWM) [12], [13], current harmonic minimum PWM (CHMPWM) [14], [15], [16], and their respective variants. SPWM and SVPWM are favored for their clear principles and ease of engineering implementation, and as such, they have been extensively researched and applied. However, the harmonic characteristics of SPWM and SVPWM are suboptimal due to the lack of consideration for system characteristics. It is usually necessary to increase the switching frequency to reduce the current harmonic. This design method, which relies on improving the switching frequency to ensure system performance, has great limitations, such as reducing the system efficiency and power density, increasing the volume and weight of heat dissipation components, shortening the service life of power devices, etc [17].

Intermediate 60° modulation is mainly used in low carrier ratio conditions, but it only ensures that the output fundamental voltage is in accordance with the voltage command without any optimization of the current harmonics [10]. SHEPWM completely eliminates a number of specified harmonics and is particularly suited to railroad traction systems because it achieves complete elimination of low-frequency torque pulsations at low switching frequencies. However, SHEPWM does not guarantee that the current total harmonic distortion (THD) is minimized,

Received 30 May 2024; revised 11 July 2024 and 7 September 2024; accepted 15 October 2024. Date of publication 23 October 2024; date of current version 18 December 2024. This work was supported by the National Natural Science Foundation of China under Grant 52177202. Recommended for publication by Associate Editor P. Karamanakos. *(Corresponding author: Fei Xiao.)*

The authors are with the National Key Laboratory of Electromagnetic Energy, Naval University of Engineering, Wuhan 430033, China (e-mail: lcq23@nue.edu.cn; m22380801@nue.edu.cn; 3150101258@zju.edu.cn; xfeyninger23@nue.edu.cn; wangrt123@nue.edu.cn; gaoshan23@nue.edu.cn; ljl23@nue.edu.cn; zvivi23@nue.edu.cn).

Color versions of one or more figures in this article are available at https://doi.org/10.1109/TPEL.2024.3485209.

Digital Object Identifier 10.1109/TPEL.2024.3485209

and the lowest uncanceled harmonic content increases significantly [18].

Current harmonic minimum pulse width modulation (CHMPWM) is a very promising PWM technique by establishing the mathematical relationship between the switching angle and the fundamental and harmonics of the current and then finding the optimal solutions to make the system have the theoretical minimum current harmonics. Earlier CHMPWM used the minimized weighted total harmonic distortion (WTHD) as the optimization objective to calculate the optimal switching angle, which is suitable for three-phase asynchronous motors and three-phase surface-mounted PMSMs [19], [20], [21]. The mathematical model of WTHD cannot describe the effect of the salient pole characteristics on the harmonic currents of the PMSM, so the literature [22] proposes the optimization index of harmonic currents of the electrically-excited synchronous motors by considering salient pole characteristics, which is also applicable to three-phase PMSMs under zero *d*-axis voltage conditions. The authors in [15] proposed a CHMPWM that simultaneously considers the salient pole characteristic and the load angle, which further broadens its applicability to PMSMs.

The mathematical model of DTP-PMSM is more complex compared to three-phase PMSM, which creates a challenge for accurate modeling of CHMPWM. A CHMPWM for DTP-PMSM was proposed in [23] and considered the effects of the salient pole ratio, the leakage inductance, and the load angle. In [24], the difference between three-phase PMSM and DTP-PMSM drives was analyzed, and a CHMPWM-based model predictive pulse pattern control (MP $^3$ C) scheme was proposed for the DTP-PMSM. The two-level inverter without output filters, which is widely used in all kinds of power electronic equipment, was employed in [23] and [24].

CHMPWM has been extensively studied in recent years [19], [20], [23], [25], [26], [27], [28], [29], [30], [31], which shows that it is quite meaningful work to study CHMPWM under different topologies, filters, and load types. In this article, CHMPWM is investigated for DTP-PMSM systems with 3L-NPC topology and various output filters, such as *L*, *LC*, *LRC*, *LCL*, and *LRCL* filters. To the best of the authors' knowledge, no similar research work is available. The proposed CHMPWM can further reduce the current harmonic content of DTP-PMSM systems, which is especially suitable for application scenarios with stringent power quality requirements, such as flywheel energy storage systems that are currently booming.

In addition, the current THD constraint is an important factor to be considered in filter design. By solving the filter parameter optimization problem considering the current THD constraint, the filter parameters with minimum cost/volume/weight can be obtained. The proposed method can accurately calculate the current THD under the specified filter parameters, which lays a valuable theoretical foundation for the optimal design of filters. However, it is important to note that designing the optimal filter is a complex task. The optimal switching angles, which influence the current THD, are contingent on the filter parameters. As a result, multiple iterations are necessary to achieve the optimal filter design.

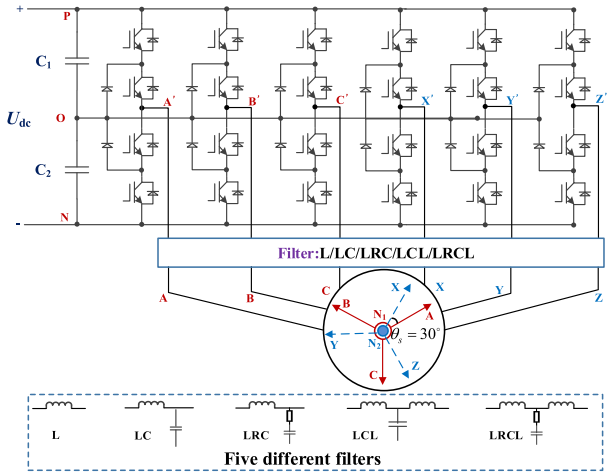


Fig. 1. Surface-mounted DTP-PMSM system based on 3L-NPC inverter with output filter.

The rest of this article is organized as follows. In Section II, the mathematical model of CHMPWM for the surface-mounted DTP-PMSM is established. In Section III, the calculation method of switching angles and performance analysis of the proposed CHMPWM are provided. In Section IV, simulation and experimental studies are performed to demonstrate the effectiveness of the proposed scheme. Finally, Section V concludes this article.

## II. Mathematical Modeling of CHMPWM for Surface-Mounted DTP-PMSM

A surface-mounted DTP-PMSM system based on a 3L-NPC inverter with an output filter is shown in Fig. 1. The DTP-PMSM is composed of ABC winding and XYZ winding, both of which are connected in a star shape, and the center points are isolated without grounding. The A phase leads the X phase by 30° electrical degree. The mathematical model of the system shown in Fig. 1 is given as

$$\mathbf{u}'_{\mathbf{sO}} = \mathbf{u}'_{\mathbf{s}} + \mathbf{u}_{\mathbf{NO}} \tag{1a}$$

$$\mathbf{u}'_{\mathbf{s}} = G^{-1}\mathbf{u}_{\mathbf{s}} \tag{1b}$$

$$\mathbf{u}_{\mathbf{s}} = \mathbf{R}_{\mathbf{s}}\mathbf{i}_{\mathbf{s}} + \frac{\mathrm{d}\boldsymbol{\Psi}_{\mathbf{s}}}{\mathrm{d}t} \tag{1c}$$

$$\boldsymbol{\Psi}_{\mathbf{s}} = \mathbf{L}_{\mathbf{s}}\mathbf{i}_{\mathbf{s}} + \gamma_{\mathbf{s}}\psi_f \tag{1d}$$

where

$$\mathbf{u}'_{\mathbf{sO}} = [u_{A'O}, u_{B'O}, u_{C'O}, u_{X'O}, u_{Y'O}, u_{Z'O}]^T \tag{2a}$$

$$\mathbf{u}'_{\mathbf{s}} = [u_{A'N_1}, u_{B'N_1}, u_{C'N_1}, u_{X'N_2}, u_{Y'N_2}, u_{Z'N_2}]^T \tag{2b}$$

$$\mathbf{u}_{\mathbf{s}} = [u_{AN_1}, u_{BN_1}, u_{CN_1}, u_{XN_2}, u_{YN_2}, u_{ZN_2}]^T \tag{2c}$$

$$\mathbf{u}_{\mathbf{NO}} = [u_{N_1O}, u_{N_1O}, u_{N_1O}, u_{N_2O}, u_{N_2O}, u_{N_2O}]^T \tag{2d}$$

$$\mathbf{i}_{\mathbf{s}} = [i_A, i_B, i_C, i_X, i_Y, i_Z]^T \tag{2e}$$

$$\boldsymbol{\Psi}_{\mathbf{s}} = [\psi_A, \psi_B, \psi_C, \psi_X, \psi_Y, \psi_Z]^T \tag{2f}$$

$$\mathbf{R}_{\mathbf{s}} = R_s\mathbf{I}_{\mathbf{6}} \tag{2g}$$

and

$$\gamma_{\mathbf{s}} = \left[\cos\theta_e, \cos\left(\theta_e - \frac{2\pi}{3}\right), \cos\left(\theta_e + \frac{2\pi}{3}\right), \cos\left(\theta_e - \frac{\pi}{6}\right), \cos\left(\theta_e - \frac{5\pi}{6}\right), \cos\left(\theta_e + \frac{\pi}{2}\right)\right]^T$$

$$\mathbf{L_s} = \begin{bmatrix} \mathbf{L_{s1s1}} & \mathbf{L_{s1s2}} \\ \mathbf{L_{s2s1}} & \mathbf{L_{s2s2}} \end{bmatrix}, \mathbf{L_{s2s2}} = \mathbf{L_{s1s1}}, \mathbf{L_{s2s1}} = \mathbf{L_{s1s2}^T}$$

$$\mathbf{L_{s1s1}} = L_{aa1}\mathbf{I_3} + L_{aadq}\begin{bmatrix} 1 & -\frac{1}{2} & -\frac{1}{2} \\ -\frac{1}{2} & 1 & -\frac{1}{2} \\ -\frac{1}{2} & -\frac{1}{2} & 1 \end{bmatrix}$$

$$\mathbf{L_{s1s2}} = L_{aadq}\begin{bmatrix} \frac{\sqrt{3}}{2} & -\frac{\sqrt{3}}{2} & 0 \\ 0 & \frac{\sqrt{3}}{2} & -\frac{\sqrt{3}}{2} \\ -\frac{\sqrt{3}}{2} & 0 & \frac{\sqrt{3}}{2} \end{bmatrix}. \tag{3}$$

In the above equations, $\mathbf{u'_{sO}}$ is the output voltage vector of the inverter relative to the inverter midpoint O. $\mathbf{u'_s}$ is the output voltage vector of the inverter relative to the neutral points $N_1$ and $N_2$ of ABC and XYZ windings. $\mathbf{u_s}$ is the phase voltage vector of the DTP-PMSM. $G$ is the transfer function, which is determined by the output filter and the motor parameters. $\mathbf{u_{NO}}$ is the voltage vector between $N_1$, $N_2$, and O. $\mathbf{i_s}$ is the phase current vector of the DTP-PMSM. $\mathbf{\Psi_s}$ is the magnetic flux vector, $\mathbf{R_s}$ is the resistance matrix, $\mathbf{L_s}$ is the inductance matrix, $\gamma_{\mathbf{s}}$ is the magnetic flux coefficient vector, $\psi_f$ is the permanent magnet flux linkage, and $R_s$ is the phase resistance. $\theta_e$ is the electrical angle, i.e., the angle between the N-pole of the rotor and the axis of the A-phase winding. $\mathbf{I_6}$ and $\mathbf{I_3}$ are the 6th and 3rd order identity matrices, respectively. $\mathbf{L_{s1s1}}$ is the inductance matrix of the ABC winding; $\mathbf{L_{s2s2}}$ represents the inductance matrix of the XYZ winding; $\mathbf{L_{s1s2}}$ and $\mathbf{L_{s2s1}}$ represent the mutual inductance matrices between the ABC and XYZ windings. $L_{aa1}$ is the leakage inductance, and $L_{aadq}$ is the main self-inductance in the $dq$-axis.

For the system shown in Fig. 1, the inverter output voltage $\mathbf{u'_{sO}}$ using CHMPWM has the characteristics of half-wave symmetry and quarter-wave symmetry and only contains $(6k \pm 1)$th harmonic $(k = 1, 2, 3, \cdots)$. Therefore, $\mathbf{u'_{sO}}$ can be described as [24]

$$u_{A'O} = \sum_{n=1,5,7,\cdots}^{\infty} U_n \sin(n\theta_1)$$

$$u_{B'O} = \sum_{n=1,5,7,\cdots}^{\infty} U_n \sin\left[n\left(\theta_1 - \frac{2\pi}{3}\right)\right]$$

$$u_{C'O} = \sum_{n=1,5,7,\cdots}^{\infty} U_n \sin\left[n\left(\theta_1 + \frac{2\pi}{3}\right)\right]$$

$$u_{X'O} = \sum_{n=1,5,7,\cdots}^{\infty} U_n \sin(n\theta_2)$$

$$u_{Y'O} = \sum_{n=1,5,7,\cdots}^{\infty} U_n \sin\left[n\left(\theta_2 - \frac{2\pi}{3}\right)\right]$$

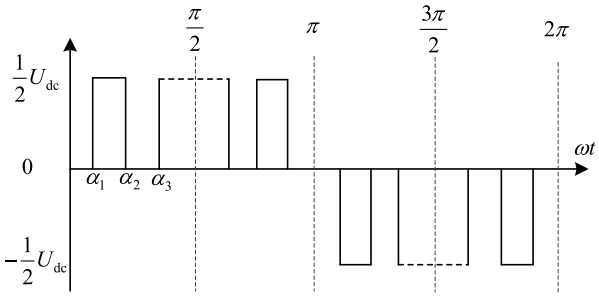


Fig. 2. A-phase voltage pulse waveform of CHMPWM.

$$u_{Z'O} = \sum_{n=1,5,7,\cdots}^{\infty} U_n \sin\left[n\left(\theta_2 + \frac{2\pi}{3}\right)\right] \tag{4}$$

where $\theta_1 = \omega_e t$, $\theta_2 = \theta_1 - \pi/6$, $\omega_e$ is the electrical angular speed, $n$ is the harmonic order, $U_n$ is the amplitude of the $n$th harmonic voltage and is expressed as [32]

$$U_n = \frac{2U_{dc}}{n\pi}\sum_{i=1}^{N}(-1)^{i+1}\cos(n\alpha_i) \tag{5}$$

where $U_{dc}$ is the dc bus voltage, $N$ is the number of switching angles between 0° and 90°, corresponding to a carrier ratio of $2N + 1$, $\alpha_i$ is the switching angle of the $i$th switching event. The waveform of the A-phase voltage pulse is shown in Fig. 2.

According to the principle of constant magnetic potential [33] and combining (1) and (4), the voltages of the DTP-PMSM under $\alpha\beta$ coordinates can be transformed to the following expressions:

$$u_{\alpha 1} = GU_1\sin\theta_1 + G\sum_{k=1}^{\infty}\{U_k^-\sin k_{\theta_1}^- + U_k^+\sin k_{\theta_1}^+\}$$

$$u_{\beta 1} = -GU_1\cos\theta_1 + G\sum_{k=1}^{\infty}\{U_k^-\cos k_{\theta_1}^- - U_k^+\cos k_{\theta_1}^+\}$$

$$u_{\alpha 2} = GU_1\sin\theta_2 + G\sum_{k=1}^{\infty}\{U_k^-\sin k_{\theta_2}^- + U_k^+\sin k_{\theta_2}^+\}$$

$$u_{\beta 2} = -GU_1\cos\theta_2 + G\sum_{k=1}^{\infty}\{U_k^-\cos k_{\theta_2}^- - U_k^+\cos k_{\theta_2}^+\} \tag{6}$$

where

$$U_k^- = U_{6k-1}, U_k^+ = U_{6k+1} \tag{7a}$$

$$k_{\theta_1}^- = (6k-1)\theta_1, k_{\theta_2}^- = (6k-1)\theta_2 \tag{7b}$$

$$k_{\theta_1}^+ = (6k+1)\theta_1, k_{\theta_2}^+ = (6k+1)\theta_2 \tag{7c}$$

and $u_{\alpha 1}, u_{\beta 1}$ are the voltages of ABC winding, and $u_{\alpha 2}, u_{\beta 2}$ are the voltages of XYZ winding.

The angular relationships in different coordinate systems are shown in Fig. 3, where $\psi_r$ is the angle between the phase voltage vector $\mathbf{u_{s1}}$ of the ABC winding and the $d$ axis. Therefore, we can get

$$\theta_e = \theta_1 - \psi_r - \frac{\pi}{2}. \tag{8}$$

As CHMPWM is mainly used at medium and high speeds, the phase resistance $R_s$ in (1) can be neglected approximately.

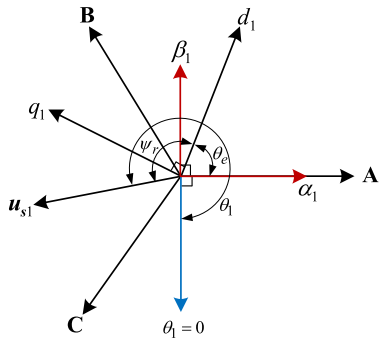


Fig. 3. Angular relationships in different coordinate systems.

Therefore, the relationship between the output current and voltage can be expressed as follows:

$$\mathbf{i_s} = \mathbf{L_s^{-1}}\left[\int(\mathbf{u_s} + \omega_e\psi_f\beta_\mathbf{s})\mathrm{d}t\right] \tag{9}$$

where

$$\beta_\mathbf{s} = \left[\sin\theta_e, \sin\left(\theta_e - \frac{2\pi}{3}\right), \sin\left(\theta_e + \frac{2\pi}{3}\right),\right.$$
$$\left., \sin\left(\theta_e - \frac{\pi}{6}\right), \sin\left(\theta_e - \frac{5\pi}{6}\right), \sin(\theta_e + \frac{\pi}{2})\right]^T. \tag{10}$$

Define the Clarke transformation matrix $\mathbf{T_{6s}}$ as

$$\mathbf{T_{6s}} = \begin{bmatrix}\mathbf{T_{3s}} & \mathbf{O_3}\\ \mathbf{O_3} & \mathbf{T_{3s}}\end{bmatrix}, \mathbf{T_{3s}} = \frac{2}{3}\begin{bmatrix}1 & -\frac{1}{2} & -\frac{1}{2}\\ 0 & \frac{\sqrt{3}}{2} & -\frac{\sqrt{3}}{2}\\ \frac{1}{2} & \frac{1}{2} & \frac{1}{2}\end{bmatrix} \tag{11}$$

where $\mathbf{O_3}$ is the third order zero matrix.

Combining (9) and (11), the relationship between the output current and voltage in $\alpha\beta$-axis can be expressed as

$$\mathbf{i}_{\alpha\beta\mathbf{o}} = \mathbf{L_1}\int\mathbf{u}_{\alpha\beta\mathbf{o}}\mathrm{d}t + \omega_e\psi_f\mathbf{M_1}\int\beta_\mathbf{s}\mathrm{d}t \tag{12}$$

where

$$\mathbf{u}_{\alpha\beta\mathbf{o}} = [u_{\alpha1}, u_{\beta1}, u_{o1}, u_{\alpha2}, u_{\beta2}, u_{o2}]^T \tag{13a}$$
$$\mathbf{i}_{\alpha\beta\mathbf{o}} = [i_{\alpha1}, i_{\beta1}, i_{o1}, i_{\alpha2}, i_{\beta2}, i_{o2}]^T \tag{13b}$$
$$\mathbf{L_1} = \mathbf{T_{6s}}\mathbf{L_s^{-1}}\mathbf{T_{6s}^{-1}}, \mathbf{M_1} = \mathbf{T_{6s}}\mathbf{L_s^{-1}} \tag{13c}$$

and $u_{o1}, u_{o2}, i_{o1}, i_{o2}$ are zero-sequence voltage and current components.

Combining (6), (8), and (12), the mathematical relationship between the output current and voltage of ABC winding in the two-phase stationary coordinate system can be derived as

$$i_{\alpha1}^F = -\frac{\sigma}{\omega_e L_{aa1}}[GU_1\cos\theta_1 - \psi_f\omega_e\sin(\psi_r - \theta_1)]$$
$$i_{\beta1}^F = -\frac{\sigma}{\omega_e L_{aa1}}[GU_1\sin\theta_1 - \psi_f\omega_e\cos(\psi_r - \theta_1)] \tag{14}$$

and

$$i_{\alpha1}^H = \frac{-G}{\omega_e L_{aa1}}\left[\sum_{k=1,3,5,\cdots}^{\infty}\left(\frac{U_k^-}{6k-1}\cos k_{\theta1}^- + \frac{U_k^+}{6k+1}\cos k_{\theta1}^+\right)\right.$$
$$\left.+\sigma\sum_{k=2,4,6,\cdots}^{\infty}\left(\frac{U_k^-}{6k-1}\cos k_{\theta1}^- + \frac{U_k^+}{6k+1}\cos k_{\theta1}^+\right)\right]$$

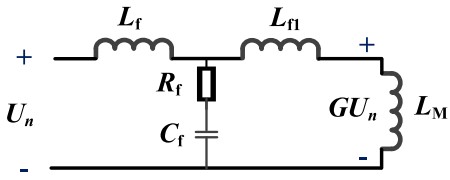


Fig. 4. Equivalent circuit of the system with the *LRCL* filter.

$$i_{\beta1}^H = \frac{G}{\omega_e L_{aa1}}\left[\sum_{k=1,3,5,\cdots}^{\infty}\left(\frac{U_k^-}{6k-1}\sin k_{\theta1}^- - \frac{U_k^+}{6k+1}\sin k_{\theta1}^+\right)\right.$$
$$\left.+\sigma\sum_{k=2,4,6,\cdots}^{\infty}\left(\frac{U_k^-}{6k-1}\sin k_{\theta1}^- - \frac{U_k^+}{6k+1}\sin k_{\theta1}^+\right)\right] \tag{15}$$

where $i_{\alpha1}^F, i_{\beta1}^F$ are the fundamental currents, $i_{\alpha1}^H, i_{\beta1}^H$ are the harmonic currents, and

$$\sigma = \frac{L_{aa1}}{L_{aa1} + 3L_{aadq}}. \tag{16}$$

According to (15), the amplitude of the $n$th harmonic current can be derived as follows:

$$i_n = \frac{GU_n}{n\omega_e L_M} \tag{17}$$

where

$$L_M = \begin{cases} L_{aa1}, \ (n = 6k \pm 1, \ k = 1, 3, 5, \cdots) \\ L_{aa1} + 3L_{aadq}, \ (n = 6k \pm 1, \ k = 2, 4, 6, \cdots) \end{cases} \tag{18}$$

The transfer function $G$ is dependent on the type of the output filter. The equivalent circuit of the system with the *LRCL* filter is shown in Fig. 4, and other types of filters can be regarded as special cases of the *LRCL* filter, such as *L*, *LC*, *LRC*, and *LCL*. According to Kirchhoff's laws, the following relationship can be derived:

$$i_n + \frac{sL_{f1}i_n + GU_n}{R_f + \frac{1}{sC_f}} = \frac{U_n - (sL_{f1}i_n + GU_n)}{sL_f} \tag{19}$$

where $L_f$ and $L_{f1}$ are the filter inductances, $R_f$ is the damping resistance, and $C_f$ is the filter capacitor. Combining (17), (18), and (19), the transfer function $G$ can be solved as follows:

$$G = \frac{B_0 s + B_1}{A_0 s^2 + A_1 s + A_2} \tag{20}$$

where

$$A_0 = C_f L_M L_f + C_f L_f L_{f1}$$
$$A_1 = C_f L_M R_f + C_f L_f R_f + C_f L_{f1} R_f$$
$$A_2 = L_M + L_f + L_{f1}$$
$$B_0 = C_f L_M R_f$$
$$B_1 = L_M. \tag{21}$$

Define $G_k^{\pm}$ as the amplitude gain of $G$ at frequency $\omega = (6k \pm 1)\omega_e$. According to (20), we have

$$G_k^{\pm} = \sqrt{\frac{(B_0\omega)^2 + B_1^2}{(A_2 - A_0\omega^2)^2 + (A_1\omega)^2}}. \tag{22}$$

Substitute (20) into (15), and we can derive the harmonic current RMS value as follows:

$$i_{RMS}^{H} = \frac{1}{\sqrt{2}\omega_e L_{aa1}} J_H \tag{23}$$

where

$$J_H = \sqrt{\sum\nolimits_{k=1,3,5,\cdots}^{\infty} C_k + \sigma^2 \sum\nolimits_{k=2,4,6,\cdots}^{\infty} C_k} \tag{24a}$$

$$C_k = \left(\frac{G_k^- U_k^-}{6k-1}\right)^2 + \left(\frac{G_k^+ U_k^+}{6k+1}\right)^2. \tag{24b}$$

To minimize the THD of all harmonic currents, the current THD is defined as

$$THD = \frac{i_{RMS}^{H}}{i_{RMS}^{F}} = \frac{1}{i_{RMS}^{F}} \frac{1}{\sqrt{2}\omega_e L_{aa1}} J_H \tag{25}$$

where $i_{RMS}^{F}$ is the RMS value of fundamental current. Considering that $1/(\sqrt{2}\omega_e L_{aa1})$ is a constant for a specified working condition and $J_H$ is proportional to the current THD. Therefore, $J_H$ can be seen as equivalent to the current THD in the steady state. Then, the mathematical model of CHMPWM for the surface-mounted DTP-PMSM system with a 3L-NPC inverter and output filters can be set up as

$$\min : J_H$$
$$s.t. : \begin{cases} \sum_{i=1}^{N} (-1)^{i+1} \cos(\alpha_i) = \frac{\pi U_1}{2U_{dc}} \triangleq m \\ 0 < \alpha_1 < \alpha_2 < \cdots < \alpha_N < \frac{\pi}{2} \end{cases} \tag{26}$$

where $m \in [0, 1]$ is the modulation ratio.

## III. Switching Angle Calculation and Performance Analysis

According to (22), (24), and the mathematical model of CHMPWM shown in (26), the optimal switching angle $\boldsymbol{\alpha}(m, \omega_e) = [\alpha_1, \alpha_2, \ldots, \alpha_N]$ depends on the modulation ratio $m$ and the fundamental frequency $\omega_e$. Algorithm 1 provides the pseudocodes for solving the optimal switching angle $\boldsymbol{\alpha}$.

### A. Performance Analysis Using an L Filter

For the convenience of comparison with the existing CHMPWM algorithms, the output filter is selected as an $L$ filter, and (22) can be simplified as

$$G_k^{\pm} = \frac{L_M}{L_M + L_f} \tag{27}$$

which is independent of $\omega_e$. In this case, the optimal switching angle only depends on the modulation ratio $m$. Rewrite (25) and (24), we can get

$$THD = \frac{1}{i_{RMS}^{F}} \frac{1}{\sqrt{2}\omega_e (L_{aa1} + L_f)} J_H \tag{28a}$$

$$J_H = \sqrt{\sum\nolimits_{k=1,3,5,\cdots}^{\infty} C_{k0} + \mu^2 \sum\nolimits_{k=2,4,6,\cdots}^{\infty} C_{k0}} \tag{28b}$$

$$C_{k0} = \left(\frac{U_k^-}{6k-1}\right)^2 + \left(\frac{U_k^+}{6k+1}\right)^2 \tag{28c}$$

$$\mu = \frac{L_{aa1} + L_f}{L_{aa1} + 3L_{aadq} + L_f}. \tag{28d}$$

**Algorithm 1:** Pseudocodes for Solving the Optimal Switching Angle of the Proposed CHMPWM.

```
\\ Harmonic order up to 200;
for ω_e = ω_e1, ω_e2, ..., ω_eM do
  for m = 0.01, 0.02, ..., 1 do
    Set J_H(m, ω_e) = ∞;
    for j = 1, 2, ..., 500 do
      Initialize α^j(m, ω_e) randomly and ensure
      0 < α_1 < α_2 < ··· < α_N < π/2;
      Solve α^j(m, ω_e) and J_H^j(m, ω_e) for the
      optimization problem (26) using the 'fmincon'
      function in Matlab;
      if J_H^j(m, ω_e) < J_H(m, ω_e) then
        Set J_H(m, ω_e) = J_H^j(m, ω_e) and
        α(m, ω_e) = α^j(m, ω_e);
      end if
    end for
  end for
end for
Store all solved optimal switching angles.
```

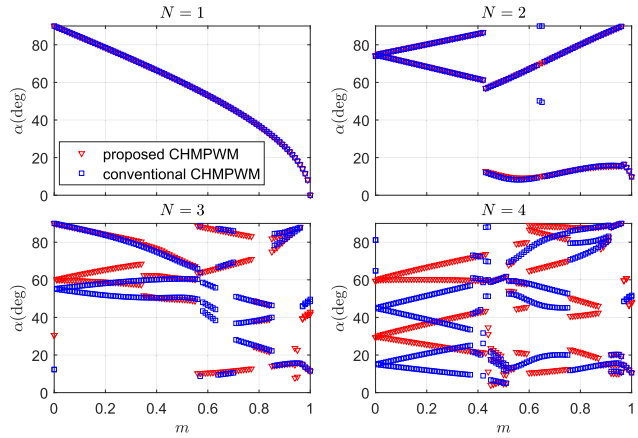


Fig. 5. Optimal switching angles of the proposed and conventional CHMPWM using an $L$ filter with different $N$.

In [20], the objective function $J_{Hconv}$ of the conventional CHMPWM was derived based on WTHD, as follows:

$$J_{Hconv} = \sqrt{\sum\nolimits_{k=1,2,3,\cdots}^{\infty} C_{k0}}. \tag{29}$$

It can be seen that compared with the objective function $J_{Hconv}$, the proposed objective function $J_H$ considers the influence of the $dq$-axis main self-inductance $L_{aadq}$ and the filter parameter $L_f$ on the current THD. Therefore, for the surface-mounted DTP-PMSM system based on the 3L-NPC inverter with output filter, the minimization of the objective functions $J_{Hconv}$ is not equivalent to minimizing the current THD. If other types of filters as shown in Fig. 1 are employed, such as *LC*, *LRC*, *LCL*, and *LRCL*, the conventional CHMPWM in [20] not only cannot minimize the current THD, but also may cause resonance problems due to the presence of filtering capacitors.

Fig. 5 shows the optimal switching angles of the proposed and conventional CHMPWM using an $L$ filter with different $N$,

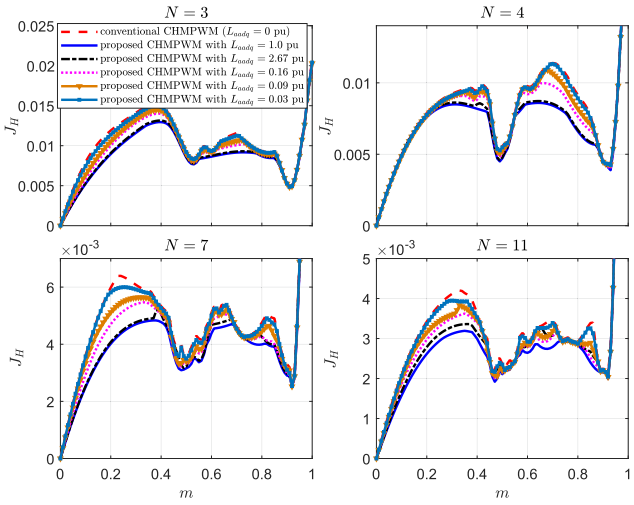


Fig. 6. Robustness of the proposed CHMPWM to the main self-inductance $L_{aadq}$ using an $L$ filter with different $N$.

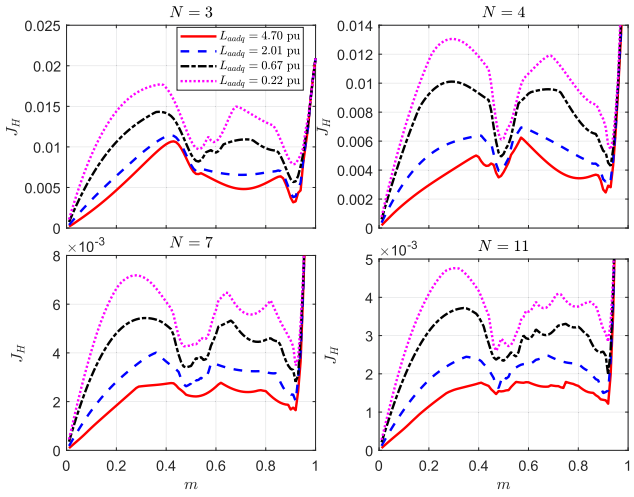


Fig. 7. Objective function value $J_H$ of the proposed CHMPWM using an $L$ filter with different $N$ and $L_{aadq}$.

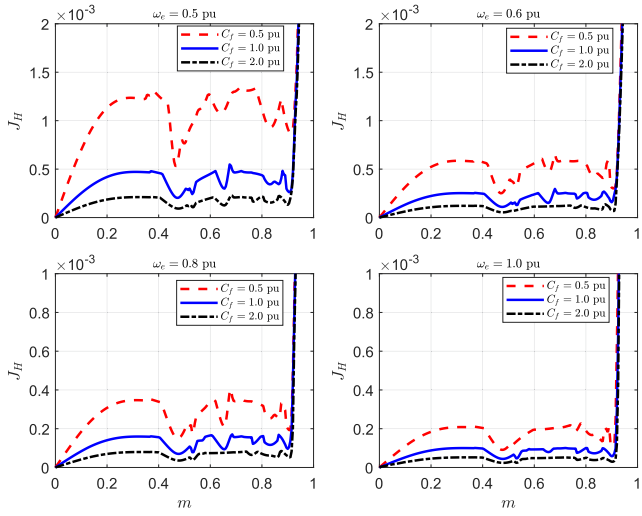


Fig. 8. Objective function value $J_H$ of the proposed CHMPWM using an *LRCL* filter under different conditions.

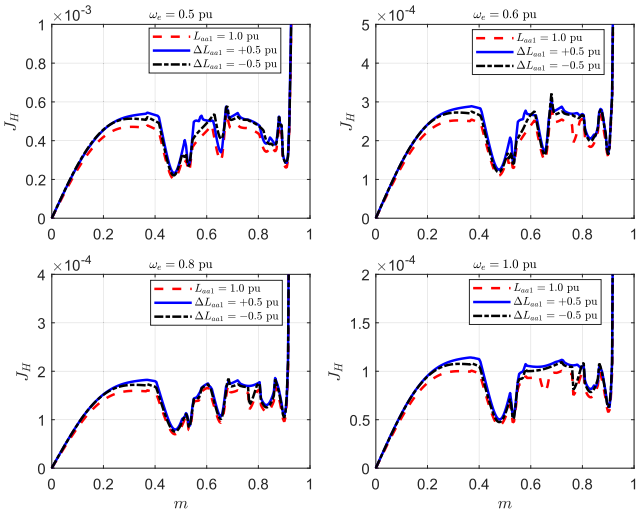


Fig. 9. Robustness of the proposed CHMPWM to leakage inductance $L_{aa1}$ using an *LRCL* filter under different conditions.

TABLE I
MAIN PARAMETERS OF THE FLYWHEEL ENERGY STORAGE SYSTEM

| Parameters | Value |
|---|---|
| Rated speed | 13000 r/min |
| Rated torque | 735 N·m |
| Rated power | 1 MW |
| Rated energy | 40 MJ |
| Rated current | 420 A |
| Number of pole pairs | 2 |
| Nominal stator resistance $R_s$ | 0.004 Ω |
| Nominal rotor PM flux linkage $\psi_f$ | 0.2045 Wb |
| Nominal leakage inductance $L_{aa1}$ | 56.87 $\mu$H |
| Nominal main self-inductance $L_{aadq}$ | 43.13 $\mu$H |
| Nominal filter inductance $L_f$ | 30 $\mu$H |
| Nominal moment of inertia of rotor | 43.2 kg·m$^2$ |
| DC link voltage | 1500 V |
| Number of switching angles $N$ | 11 |

where the results of the proposed CHMPWM are obtained based on the DTP-PMSM system parameters shown in Table I. It can be seen that the optimal switching angles of the two methods are discontinuous throughout the entire modulation ratio range in the $N \geq 2$ case. Moreover, the optimal switching angles of the two methods are consistent when $N = 1$. As $N$ increases, the distribution difference of the switching angles gradually increases.

The objective function value defined in (28b) depends on the parameter $\mu$, which is decided by $L_{aadq}$, $L_{aa1}$, and $L_f$ according to (28d). Fig. 6 provides the robustness of the proposed CHMPWM to the main self-inductance $L_{aadq}$ using an $L$ filter with different $N$ based on the parameters listed in Table I. The objective function values are all calculated via (28b) using $L_{aadq} = 1.0$ p.u., which is the actual evaluation of harmonic characteristics. In the $L_{aadq} = 1.0$ p.u. case, the $J_H$ value of the proposed method is significantly smaller than that of the

TABLE II
FILTER PARAMETERS AND CHARACTERISTICS

| Types | Parameters | | | | Characteristics for $k = 1, 3, 5, \cdots$ | | | Characteristics for $k = 2, 4, 6, \cdots$ | | |
|---|---|---|---|---|---|---|---|---|---|---|
| | $L_f/\mu$H | $R_f/m\Omega$ | $C_f/\mu$F | $L_{f1}/\mu$H | $F_{re}$/kHz | $M_{re}$/dB | $F_c$/kHz | $F_{re}$/kHz | $M_{re}$/dB | $F_c$/kHz |
| *LC* | 30 | 1.1 | 70 | 0 | 4.29 | 49.97 | 6.67 | 3.74 | 53.55 | 5.81 |
| *LRC* | 30 | 31.1 | 70 | 0 | 4.29 | 20.96 | 6.67 | 3.74 | 24.53 | 5.82 |
| *LCL* | 30 | 1.1 | 70 | 30 | 4.03 | 47.95 | 6.26 | 3.71 | 52.50 | 5.76 |
| *LRCL* | 30 | 31.1 | 70 | 30 | 4.03 | 18.94 | 6.26 | 3.70 | 23.49 | 5.76 |

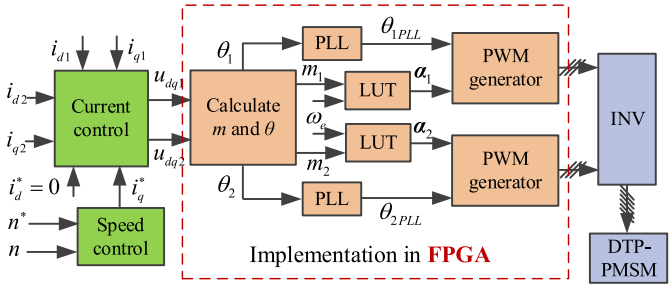


Fig. 10. System control structure diagram.

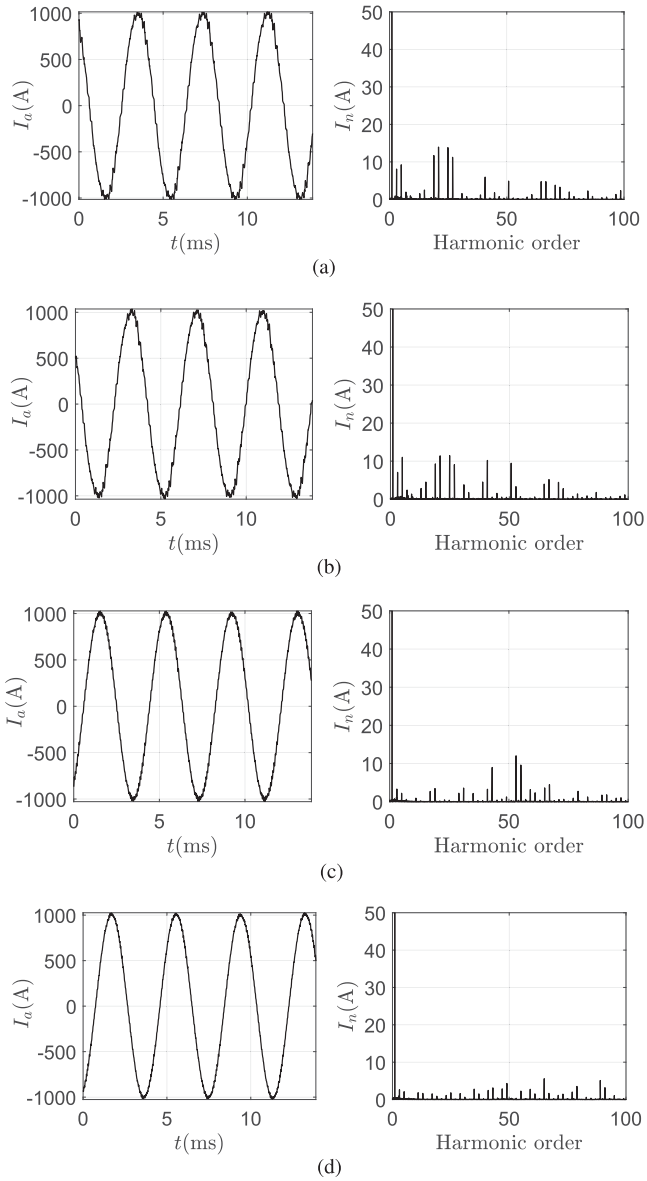


Fig. 11. Performance comparison of different modulation strategies at speed $n = 0.5$ p.u. (a) SPWM (THD=3.84%). (b) SVPWM (THD=3.78%). (c) Conventional CHMPWM (THD=2.57%). (d) The proposed CHMPWM (THD=1.84%).

conventional method, and even in some modulation ratio intervals, the reduction amplitude approaches 50%, which means that the new method can significantly reduce the harmonic content. Moreover, it can be seen that even when mismatched parameters are used to calculate the optimal switching angles, the actual objective function value $J_H$ is still less than the conventional CHMPWM, which shows that the proposed method has favorable robustness.

Further analysis shows that as $L_{aadq}$ is close to 0, the $J_H$ value also gradually approaches the objective function value of the conventional CHMPWM. However, this change is not linear relative to $L_{aadq}$. Taking the case of $L_{aadq} = 0.03$ p.u. as an example, when $N = 3$ or $N = 4$, the $J_H$ value is very close to that of the conventional CHMPWM. However, when $N = 7$ or $N = 11$, there is a significant deviation from the $J_H$ value of the conventional CHMPWM near $m = 0.3$. This phenomenon is indeed difficult to explain accurately. One possible reason is that the mathematical model of CHMPWM is rather complex, especially when the number of switching angles $N$ is large, its complexity is further increased. In some cases, even if the two sets of parameters $L_{aadq}$ are close, the optimal solutions and the corresponding objective function value $J_H$ may have significant differences.

Fig. 7 shows the objective function value $J_H$ of the proposed CHMPWM using an *L* filter with different $N$ and $L_{aadq}$. It is obvious that $J_H$ is inversely proportional to the main self-inductance $L_{aadq}$, which means that the harmonic content increases with the decrease of $L_{aadq}$.

### *B. Performance Analysis Using an LRCL Filter*

Fig. 8 shows the objective function value $J_H$ of the proposed CHMPWM using an *LRCL* filter under different conditions, in which the base values of the fundamental frequency $\omega_e$ and the *LRCR* filter parameters are shown in Tables I and II, respectively. When the filter capacitance $C_f$ of the *LRCR* filter is increased, the cutoff frequency decreases and the harmonic suppression ability is enhanced by the characteristics of the filter, so that the objective function value $J_H$ decreases with the increase of $C_f$. In addition, as $\omega_e$ increases, the harmonic frequencies increase simultaneously and the harmonic can be more easily filtered out

due to the constant cutoff frequency of the filter. Therefore, when the filter parameters remain unchanged, the objective function value $J_H$ decreases as $\omega_e$ increases.

Fig. 9 provides the robustness of the proposed CHMPWM to leakage inductance $L_{aa1}$ using an *LRCL* filter under different conditions, in which the base values of $\omega_e$, the leakage inductance $L_{aa1}$ and the *LRCR* filter parameters are listed in Tables I and II. Define $\hat{L}_{aa1}$ as the mismatched leakage inductance and $\Delta L_{aa1} = L_{aa1} - \hat{L}_{aa1}$. It can be seen that the objective function $J_H$ is close to the optimal value when the leakage inductance $L_{aa1}$ has a mismatch of +0.5 p.u. or $-0.5$ p.u. at different fundamental frequencies. This indicates that the proposed CHMPWM has good robustness to $L_{aa1}$.

In addition, compared to SPWM and SVPWM, the main limitations of CHMPWM are manifested in the following four aspects.

1) The implementation in engineering is more complex and its dynamic performance is not as good as that of SPWM and SVPWM.
2) It can only be applied under medium to high rotational speeds.
3) When the type or parameters of the load change, it may be necessary to recalculate the optimal switching angles.
4) Storing the optimal switching angles requires a certain amount of memory resources.

However, the main advantage of CHMPWM is that it has the minimum current THD at the same carrier ratio, which is of great significance for some applications that require low current THD.

## IV. Simulation and Experimental Studies

In the simulation and experimental studies, a flywheel energy storage system with a capacity of 1 MW/40MJ is taken as the research object. The main parameters are listed in Table I. Since the system has high requirements for current harmonics and takes into account constraints such as heat dissipation and efficiency, the number of switching angles is selected as 11.

Fig. 10 provides the system control structure diagram. Speed control and current control are implemented in Digital Signal Processing, while the CHMPWM algorithm is implemented in Field-Programmable Gate Array (FPGA). The subscripts "1" and "2", respectively, denote the corresponding state variables of the two sets of windings in the ABC and XYZ frames. The phase-locked loop (PLL) is used to achieve high-precision reconstruction of the position signal, thereby enhancing the performance of CHMPWM [34]. The optimal switching angle $\boldsymbol{\alpha}$ is calculated offline by Algorithm 1. When the output filter has a filtering capacitor, $\boldsymbol{\alpha}$ is a function of the modulation ratio $m$ and the electrical angular velocity $\omega_e$. When an L filter is used, $\boldsymbol{\alpha}$ is solely determined by $m$. $\boldsymbol{\alpha}$ is stored in a table format in the flash memory, and is obtained through the table lookup method in practical applications. Ultimately, the drive pulses are generated by the PWM generator.

Compared to SPWM and SVPWM, the implementation complexity of the proposed CHMPWM is primarily manifested in three aspects. First, it needs to calculate the optimal switching

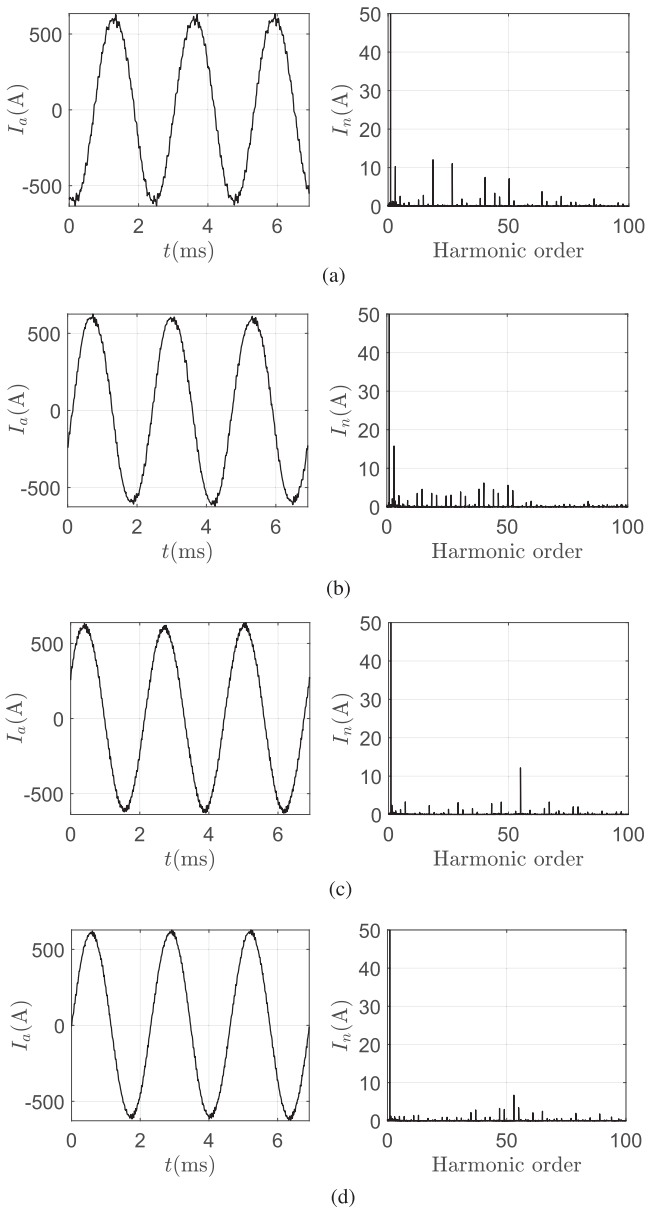


Fig. 12. Performance comparison of different modulation strategies at speed $n = 1.0$ p.u. (a) SPWM (THD=3.88%). (b) SVPWM (THD=3.20%). (c) Conventional CHMPWM (THD=2.95%). (d) The proposed CHMPWM (THD=2.34%).

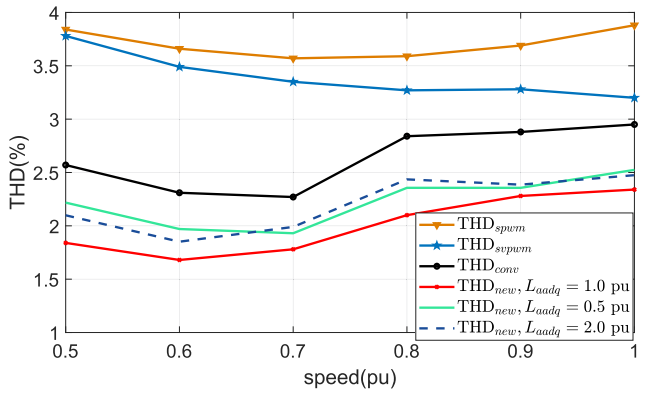


Fig. 13. Robustness of the proposed CHMPWM to system parameters.

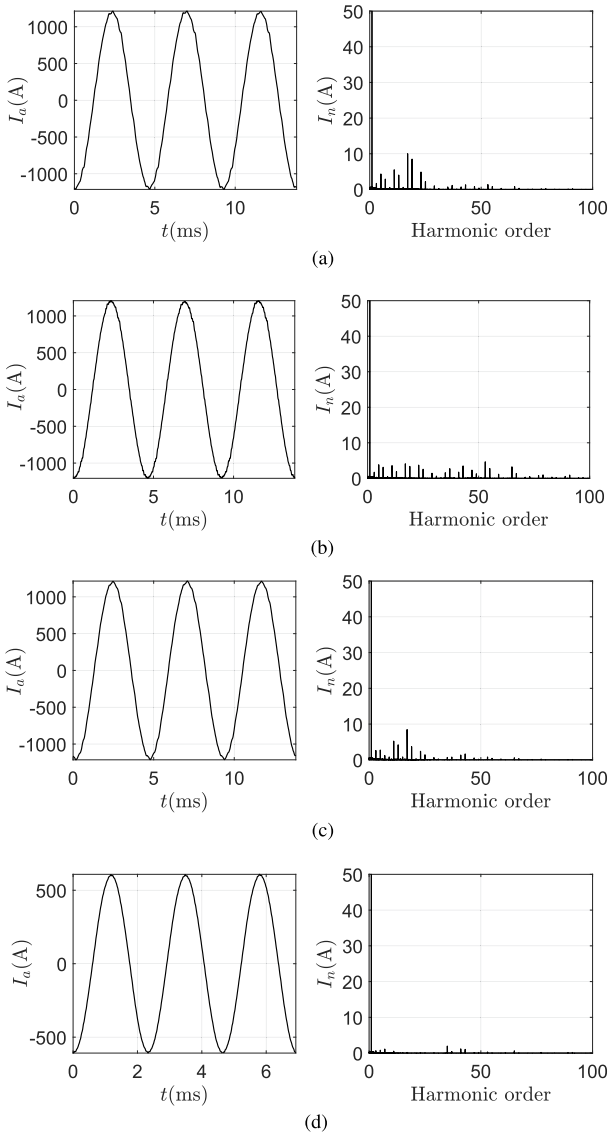


Fig. 14. Performance comparison with different types of filters at speed $n = 0.5$ p.u. (a) *LC* (THD=1.48%). (b) *LRC* (THD=1.17%). (c) *LCL* (THD=1.16%). (d) *LRCL* (THD=0.74%).

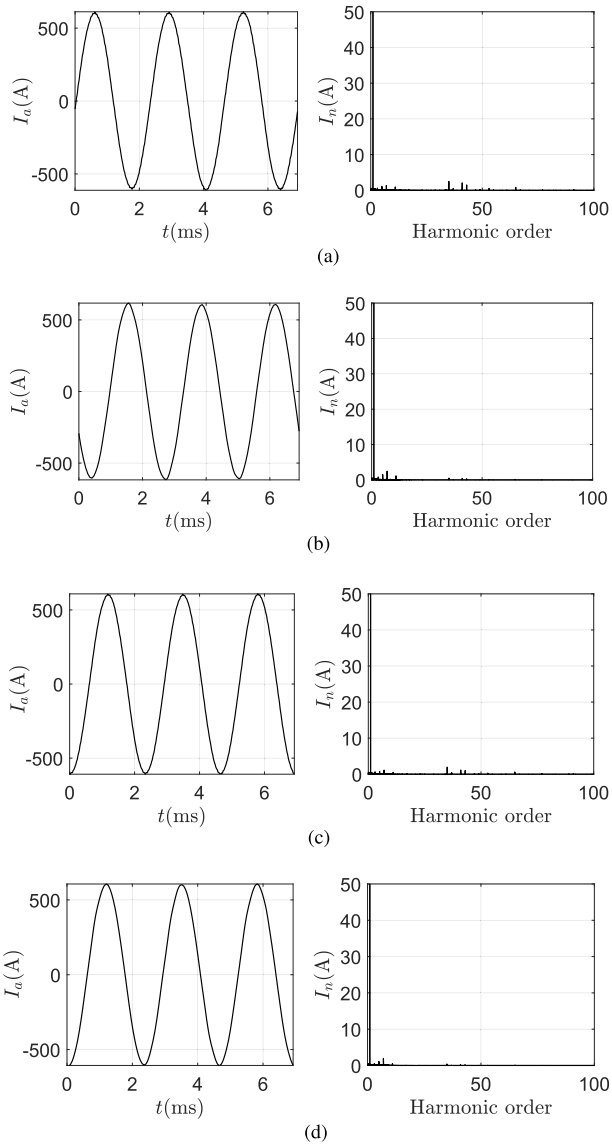


Fig. 15. Performance comparison with different types of filters at speed $n = 1.0$ p.u. (a) *LC* (THD=1.18%). (b) *LRC* (THD=0.93%). (c) *LCL* (THD=0.88%). (d) *LRCL* (THD=0.72%).

angle offline and recalculate it when the load type or parameters change. Then, in terms of engineering implementation, the optimal switching angles need to be stored in flash memory and obtained in real-time through a look-up table, which will take up some storage resources. Taking $N$=11 as an example, when the step size of the modulation ratio $m$ is 0.01 and an *L* filter is used, at least 2200 b of storage space is required. More storage space will be occupied when there are filter capacitors, depending on the choice of the step size of the electrical angular velocity $\omega_e$. Finally, a PLL is used in the implementation to improve the performance of the CHMPWM, which also consumes some computational resources.

### *A. Simulation Results With an L Filter*

The performance of the proposed CHMPWM, SPWM, SVPWM, and conventional CHMPWM is analyzed and evaluated when an *L* filter is used. The carrier ratio for both SPWM and SVPWM is 23, and the number of switching angles for both the conventional and the proposed CHMPWM is 11. The four PWM strategies have the same equivalent switching frequency.

Figs. 11 and 12 show the performance comparison of current waveforms and harmonic content of the four modulation strategies under different operating conditions. At speed $n = 0.5$ p.u., the current THD content of SPWM, SVPWM, the conventional CHMPWM, and the proposed CHMPWM are 3.84%, 3.78%, 2.57%, and 1.84%, respectively. At speed $n = 1.0$ p.u., they are 3.88%, 3.20%, 2.95%, and 2.34%, respectively.

According to the objective function (24a), it can be seen that the optimization results of the proposed CHMPWM depend on the accuracy of the parameter $\mu$ defined in (28d), which is decided by $L_f, L_{aa1}$, and $L_{aadq}$. Considering that parameter $\mu$

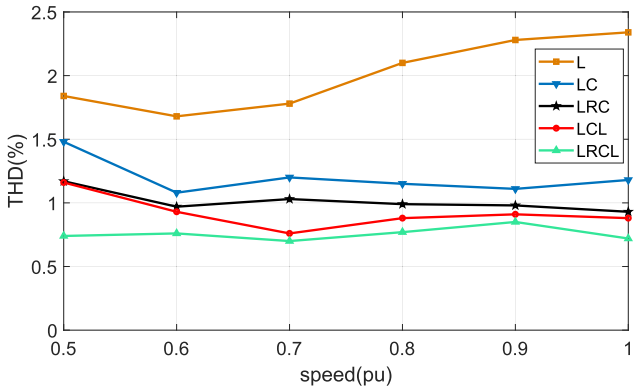


Fig. 16. Current THD comparison for the five types of filters from speed $n = 0.5$ p.u. to $n = 1.0$ p.u.

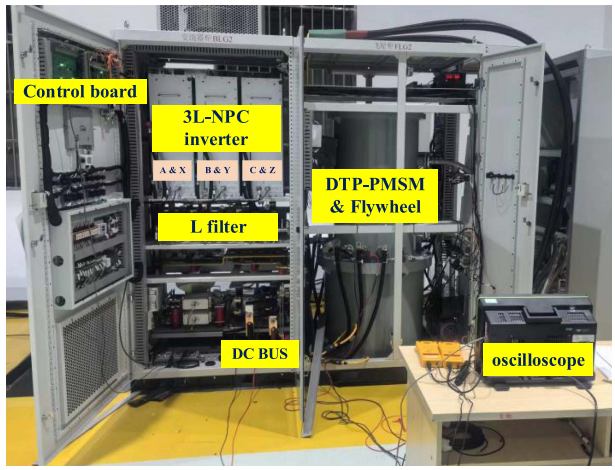


Fig. 17. Experimental platform.

can be varied between 0 and 1 by varying $L_{aadq}$, the robustness of the proposed CHMPWM to parameter $L_{aadq}$ is investigated, just as shown in Fig. 13. When the parameter $L_{aadq}$ is accurate, the current THD of the proposed CHMPWM is reduced by an average of 46%, 40%, and 24% compared to SPWM, SVPWM, and the conventional CHMPWM from speed $n = 0.5$ p.u. to $n = 1.0$ p.u., respectively. When parameter $L_{aadq}$ has a deviation of $-50\%$ or $+100\%$, the current THD of the proposed CHMPWM is still significantly smaller than the other three traditional modulation strategies.

### B. Simulation Results With Other Types of Filters

Simulation studies are carried out for other types of filters. The filter parameters and characteristics are shown in Table II, including *LC*, *LRC*, *LCL*, and *LRCL*. The optimal filter parameter design needs to comprehensively consider constraints such as cost, volume and weight, filtering effect, reactive current, damping resistance loss, resonant frequency, and so on. The design process is complex and not the focus of this article, so it is not introduced in detail. The filter parameters given in Table II are simple and feasible combinations, mainly to verify the performance of the proposed CHMPWM under different filters. The internal resistance of the filter capacitor is 1.1 mΩ, and $F_{re}$, $M_{re}$, and $F_c$ are the resonant frequency, resonant peak, and cutoff frequency respectively. In combination with Fig. 4 and (18), it can be seen that the filter characteristics are related to the harmonic order, which is the main difference from traditional filters. The optimal switching angles are calculated according to Algorithm 1 and the step size of the electrical angular velocity $\omega_e$ is selected as 0.05 p.u.

Figs. 14 and 15 show the performance comparison with different types of filters under different operating conditions. At speed $n = 0.5$ p.u., the current THD content using *LC*, *LRC*, *LCL*, and *LRCL* filters are 1.48%, 1.17%, 1.16%, and 0.74%, respectively. At speed $n = 1.0$ p.u., they are 1.18%, 0.93%, 0.88%, and 0.72%, respectively. The proposed CHMPWM can suppress the harmonic around the resonance frequency even without damping resistors. The current THD is further reduced with the use of damping resistors.

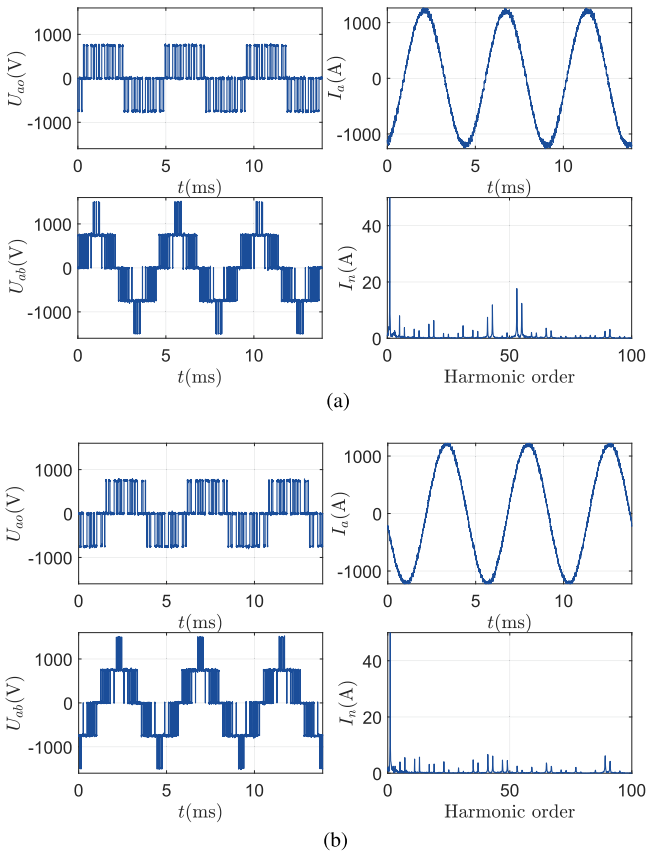


Fig. 18. Experimental results at speed $n = 0.5$ p.u. (a) Conventional CHMPWM (THD=3.51%). (b) The proposed CHMPWM (THD=2.42%).

Fig. 16 provides the current THD comparison for the five types of filters from speed $n = 0.5$ p.u. to $n = 1.0$ p.u. It can be seen that the current THD content of the *L* filter is the largest. When a filter capacitor is used, the current THD is less than 1.5%, especially the current THD of the *LRCL* filter is less than 1%.

Given that the optimal switching angles are influenced by the filter parameters, the patterns applied for each filter are different.

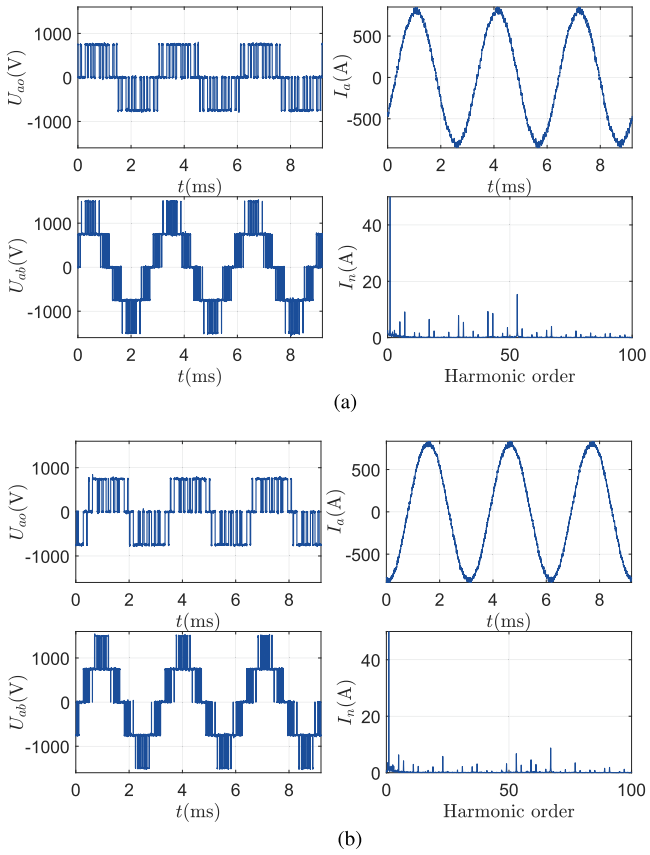


Fig. 19. Experimental results at speed $n = 0.75$ p.u. (a) Conventional CHMPWM (THD=3.30%). (b) The proposed CHMPWM (THD=2.45%).

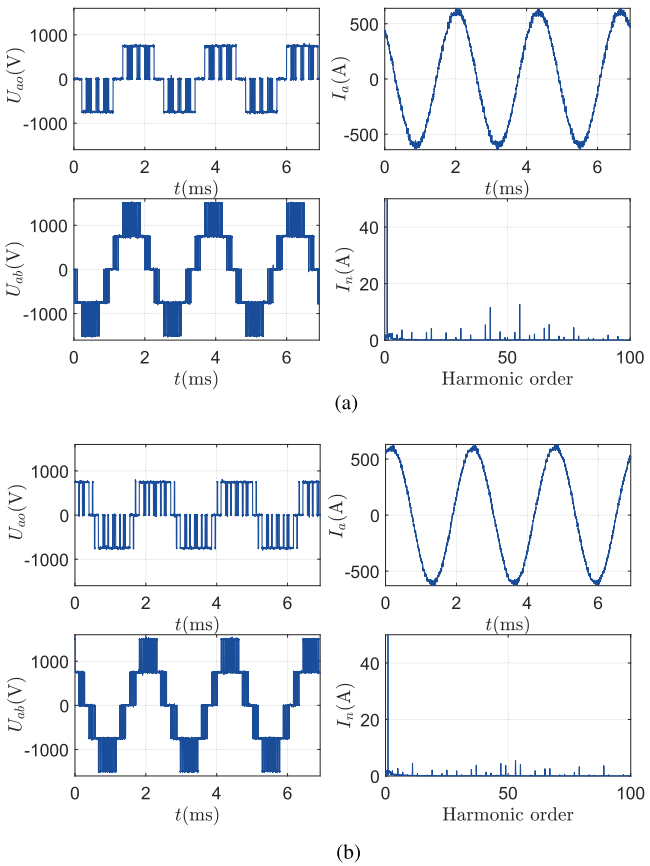


Fig. 20. Experimental results at speed $n = 1.0$ p.u. (a) Conventional CHMPWM (THD=4.27%). (b) The proposed CHMPWM (THD=2.73%).

Consequently, the comparisons presented in Figs. 14, 15, and 16 are useful only for selecting between different types of filters.

### C. Experimental Results

The flywheel energy storage system consists of an inverter with dual three-phase 3L-NPC topology, an $L$ filter, and a surface-mounted DTP-PMSM. It is mainly used in rail transportation, power grid frequency modulation, and other fields. The accompanying test equipment mainly includes an oscilloscope and a computer. The entire experimental platform is shown in Fig. 17. When the flywheel energy storage system is charged or discharged at rated power, its speed always changes, so there is no real steady state. Considering that the flywheel has a large moment of inertia (43.2 kg·m$^2$) and the speed changes very slowly, the system can be considered to be in an approximate steady state in several fundamental wave periods, and the output current can be analyzed by Fourier transform.

Figs. 18, 19, and 20 show the experimental results of the conventional CHMPWM and the proposed CHMPWM under three different working conditions. At speeds of 0.5 p.u., 0.75 p.u., and 1.0 p.u., the current THD of the conventional CHMPWM is 3.51%, 3.30%, and 4.27%, respectively. The current THD of the proposed CHMPWM is 2.42%, 2.45%, and 2.73%, respectively. Compared with the conventional CHMPWM, the proposed CHMPWM has a smaller current THD and a relatively even harmonic distribution with smaller single-current harmonics.

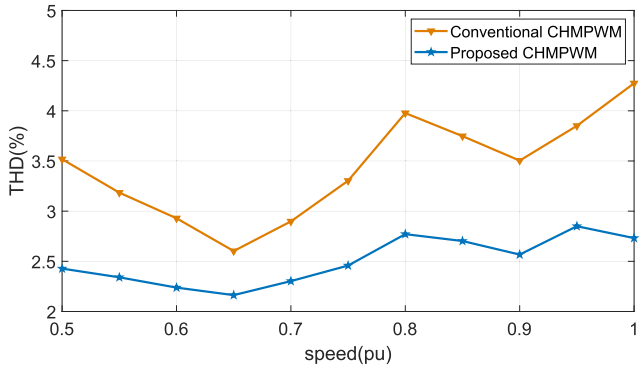


Fig. 21. Current THD comparison from speed $n = 0.5$ p.u. to $n = 1.0$ p.u.

Fig. 21 provides the current THD comparison of the conventional CHMPWM and the proposed CHMPWM from speed $n = 0.5$ p.u. to $n = 1.0$ p.u. It can be seen that the proposed CHMPWM always has a smaller current THD and is reduced by an average of 26% compared to conventional CHMPWM, which is very close to the simulation result of 24%.

It should be noted that the current THD of the actual system is higher than the simulation results, which is mainly caused by three factors: 1) mismatch of system parameters; the parameters used for simulation are matched with the set system parameters.

However, when the parameters used for the experiment do not match the actual system parameters, the harmonic characteristics of the CHMPWM degrade, as shown in Figs. 6 and 13. In addition, the performance of the current controller designed based on the motor parameters cannot be optimized; 2) dead time effect. The dead time compensation algorithm based on current polarity judgment is used in both simulation and experiment. However, due to the current sensor accuracy, sampling delay, and other factors, the current information obtained in the experiment is not as accurate as in the simulation, which in turn reduces the dead time compensation effect and increases the current harmonic content; 3) the delay of the actual control system. It mainly includes the sampling link delay of motor current and rotor position, communication delay between master and slave controllers, etc., which will negatively affect the control performance and the current THD.

In summary, compared with SPWM, SVPWM, and the conventional CHMPWM, the proposed CHMPWM can further reduce the current harmonics, and it is of great significance to improve power quality, reduce harmonic loss, and improve the comprehensive performance of the system.

## V. Conclusion

This article proposes a novel CHMPWM suitable for the surface-mounted DTP-PMSM system with a 3L-NPC inverter and an output filter. The primary difference between the proposed method and conventional CHMPWM lies in the consideration of the system parameters, which theoretically results in superior harmonic characteristics. Simulation and experimental results indicate that the proposed method significantly reduces the current harmonic content compared to SPWM, SVPWM, and conventional CHMPWM while also demonstrating good robustness to system parameters. Future work will primarily include the analysis of the dead time effect and minimum pulse width limitation on current harmonic properties, along with the development of compensation methods. In addition, the performance analysis of the modulation strategy under high-dynamic operating conditions will be conducted.

## References


[1] M. Gu, Z. Wang, and B. Wang, "Optimization of torque ripple for low-carrier-ratio dual three-phase PMSM with pulse pattern control," *IEEE Trans. Power Electron.*, vol. 38, no. 12, pp. 15091–15096, Dec. 2023.

[2] Y. Liu et al., "Direct torque control schemes for dual three-phase PMSM considering unbalanced DC-link voltages," *IEEE Trans. Energy Convers.*, vol. 39, no. 1, pp. 229–242, Mar. 2024.

[3] L. Lu, Y. Mao, X. Wang, L. Jin, and Z. Wang, "Maximum-torque optimization control of dual three-phase PMSM in low-frequency and static operations," *IEEE Trans. Emerg. Sel. Topics Power Electron.*, vol. 11, no. 5, pp. 5268–5278, Oct. 2023.

[4] Y. Li, Y. Hu, and Z. Q. Zhu, "Current harmonics and unbalance suppression of dual three-phase PMSM based on adaptive linear neuron controller," *IEEE Trans. Energy Convers.*, vol. 38, no. 4, pp. 2353–2363, Dec. 2023.

[5] B. Zheng, J. Zou, Y. Xu, G. Yu, L. Wang, and P. Zanchetta, "High-frequency current harmonic analysis and suppression in dual three-phase PMSMs with advanced carrier phase-shift PWM," *IEEE Trans. Power Electron.*, vol. 39, no. 2, pp. 2569–2581, Feb. 2024.

[6] Z. Liu, Z. Zheng, S. D. Sudhoff, C. Gu, and Y. Li, "Reduction of common-mode voltage in multiphase two-level inverters using SPWM with phase-shifted carriers," *IEEE Trans. Power Electron.*, vol. 31, no. 9, pp. 6631–6645, Sep. 2016.

[7] H. Li, Z. Yang, B. Wang, V. G. Agelidis, and B. Zhang, "On thermal impact of chaotic frequency modulation SPWM techniques," *IEEE Trans. Ind. Electron.*, vol. 64, no. 3, pp. 2032–2043, Mar. 2017.

[8] S. Pan, J. Pan, and Z. Tian, "A shifted SVPWM method to control DC-link resonant inverters and its FPGA realization," *IEEE Trans. Ind. Electron.*, vol. 59, no. 9, pp. 3383–3391, Sep. 2012.

[9] Q. Yan, Z. Zhou, M. Wu, X. Yuan, R. Zhao, and H. Xu, "A simplified analytical algorithm in abc coordinate for the three-level SVPWM," *IEEE Trans. Power Electron.*, vol. 36, no. 4, pp. 3622–3627, Apr. 2021.

[10] W. Zhang, W. Yao, and Z. Song, "Intermediate 60° modulation with real-time gain correction based on phase-shifted carrier," in *Proc. 2022 IEEE Int. Power Electron. Appl. Conf. Expo.*, 2022, pp. 501–505.

[11] T. Bhavsar and G. Narayanan, "Harmonic analysis of advanced bus-clamping PWM techniques," *IEEE Trans. Power Electron.*, vol. 24, no. 10, pp. 2347–2352, Oct. 2009.

[12] M. Balasubramonian and V. Rajamani, "Design and real-time implementation of SHEPWM in single-phase inverter using generalized hopfield neural network," *IEEE Trans. Ind. Electron.*, vol. 61, no. 11, pp. 6327–6336, Nov. 2014.

[13] M. Zabaleta, E. Burguete, D. Madariaga, I. Zubimendi, M. Zubiaga, and I. Larrazabal, "LCL grid filter design of a multimegawatt medium-voltage converter for offshore wind turbine using SHEPWM modulation," *IEEE Trans. Power Electron.*, vol. 31, no. 3, pp. 1993–2001, Mar. 2016.

[14] W. Song, J. Feng, S. Jiang, and H. Wang, "Current harmonic minimum pulse-width modulation for ANPC-5 L inverter," in *Proc. 2014 17th Int. Conf. Elect. Mach. Syst.*, 2014, pp. 1425–1429.

[15] Z. Zhang, X. Ge, Z. Tian, X. Zhang, Q. Tang, and X. Feng, "A PWM for minimum current harmonic distortion in metro traction PMSM with saliency ratio and load angle constrains," *IEEE Trans. Power Electron.*, vol. 33, no. 5, pp. 4498–4511, May 2018.

[16] B. Guan and S. Doki, "A current harmonic minimum PWM for three-level converters aiming at the low-frequency fluctuation minimum of neutral-point potential," *IEEE Trans. Ind. Electron.*, vol. 66, no. 5, pp. 3380–3390, May 2019.

[17] A. Edpuganti and A. K. Rathore, "A survey of low switching frequency modulation techniques for medium-voltage multilevel converters," *IEEE Trans. Ind. Appl.*, vol. 51, no. 5, pp. 4212–4228, Sep./Oct. 2015.

[18] Z. Liu and B. Guan, "Active optimization method for power loss distribution in t-type three-level converter under half-wave symmetry SHEPWM," *IEEE Trans. Ind. Electron.*, vol. 70, no. 10, pp. 9731–9740, Oct. 2023.

[19] D. G. Holmes and T. A. Lipo, *Pulse Width Modulation for Power Converters: Principles and Practice*. New York, NY, USA: IEEE Press, 2003.

[20] A. Tripathi and G. Narayanan, "Investigations on optimal pulse width modulation to minimize total harmonic distortion in the line current," *IEEE Trans. Ind. Appl.*, vol. 53, no. 1, pp. 212–221, Jan./Feb. 2017.

[21] F. Mink, K. Peter, H. Kasten, and S. Beineke, "Feedback control of high-speed PMSM with synchronous optimal PWM," in *Proc. 2016 18th Eur. Conf. Power Electron. Appl.*, 2016, pp. 1–10.

[22] A. S. A. R. Rezazade and M. Aflaki, "Modulation error observation and regulation for use in off-line optimal PWM fed high power synchronous motors," in *Proc. 1st Ind. Electron. Appl.*, 2006, pp. 1–8.

[23] G. Liang et al., "An optimized pulsewidth modulation for dual three-phase PMSM under low carrier ratio," *IEEE Trans. Power Electron.*, vol. 37, no. 3, pp. 3062–3072, Mar. 2022.

[24] M. Gu, Z. Wang, P. Liu, and J. He, "Comparative study of advanced modulation and control schemes for dual three-phase PMSM drives with low switching frequencies," *IEEE Trans. Transport. Electrific.*, vol. 10, no. 1, pp. 962–975, Mar. 2024.

[25] T. Dorfling, H. d. T. Mouton, and T. Geyer, "Generalized model predictive pulse pattern control based on small-signal modeling–Part 2: Implementation and analysis," *IEEE Trans. Power Electron.*, vol. 37, no. 9, pp. 10488–10498, Sep. 2022.

[26] S. Rahmanpour, P. Karamanakos, and T. Geyer, "Three-level optimized pulse patterns for grid-connected converters with LCL filters," in *Proc. 2023 IEEE Energy Convers. Congr. Expo.*, 2023, pp. 1430–1437.

[27] A. Birda, J. Reuss, and C. M. Hackl, "Synchronous optimal pulsewidth modulation for synchronous machines with highly operating point dependent magnetic anisotropy," *IEEE Trans. Ind. Electron.*, vol. 68, no. 5, pp. 3760–3769, May 2021.

[28] N. Hartgenbusch, R. W. De Doncker, and A. Thünen, "Optimized pulse patterns for salient synchronous machines," in *Proc. 2020 23rd Int. Conf. Elect. Mach. Syst.*, 2020, pp. 359–364.

[29] G. Darivianakis and I. Tsoumas, "Insight into the peculiarities of optimized pulse patterns for permanent-magnet synchronous machines," in *Proc. 2020 22nd Eur. Conf. Power Electron. Appl.*, 2020, pp. P.1–P.8.

[30] M. Hepp, M. Saur, W. Wondrak, and M.-M. Bakran, "Optimized pulse patterns for salient permanent magnet synchronous machines considering nonlinear magnetic effects," in *Proc. PCIM Europe 2023; Int. Exhib. Conf. Power Electron., Intell. Motion, Renewable Energy Energy Manage.*, 2023, pp. 1–10.
[31] E. Kontodinas, P. Karamanakos, A. Kraemer, and S. Wendel, "Optimized pulse patterns for synchronous machines with non-sinusoidal back-EMF," in *Proc. 2023 25th Eur. Conf. Power Electron. Appl.*, 2023, pp. 1–9.
[32] A. Sanchez-Ruiz et al., "DC-link neutral point control for 3L-NPC converters utilizing selective harmonic elimination PWM," *IEEE Trans. Ind. Electron.*, vol. 69, no. 9, pp. 8633–8644, Sep. 2022.
[33] R. Krishnan, *Permanent Magnet Synchronous and Brushless DC Motor Drives*. Boca Raton, FL, USA: CRC Press, 2010.
[34] J. Liu, W. Zhang, F. Xiao, C. Lian, and S. Gao, "Six-step mode control of IPMSM for railway vehicle traction eliminating the DC offset in input current," *IEEE Trans. Power Electron.*, vol. 34, no. 9, pp. 8981–8993, Sep. 2019.

**Chuanqiang Lian** received the B.S. degree in automation from the Department of Automation, Tsinghua University, Beijing, China, in 2008, and the M.S. and Ph.D. degrees in control science and engineering from the College of Mechatronic Engineering and Automation (CMA), National University of Defense Technology (NUDT), Changsha, China, in 2010 and 2016, respectively.

He is currently an Associate Professor with the National Key Laboratory of Electromagnetic Energy, Naval University of Engineering, Wuhan, China. He has authored or coauthored more than twenty papers in international journals and conferences. His current research interests include ac motor control and flywheel energy storage.

**LiYuan Guo** was born in Shanxi province, China, in 1999. He received the B.S. degree in electrical engineering from Shanxi University, Taiyuan, China, in 2022. He is currently working toward the M.S. degree in electrical engineering with the National Key Laboratory of Electromagnetic Energy, Naval University of Engineering, Wuhan, China.

His current research interests include high-performance control of permanent magnet synchronous motors.

**GuanDa Xu** was born in Jiangxi province, China, in 1998. He received the B.S. degree in electrical engineering from Zhejiang University, Hangzhou, China, in 2019, and the M.S. degree in electrical engineering from the Naval University of Engineering, Wuhan, China, in 2021. He is currently working toward the Ph.D. degree in electrical engineering with the National Key Laboratory of Electromagnetic Energy, Naval University of Engineering, Wuhan, China.

His research interests include position and current sensorless control of ac motors and electric vehicle drives.

**Fei Xiao** was born in Hubei province, China, in 1977. He received the B.S. and M.S. degrees in electrical engineering from the Naval University of Engineering, Wuhan, China, in 1999 and 2001, respectively, and the Ph.D. degree in electrical engineering with Zhejiang University, Hangzhou, China, in 2012.

From 2003 to 2009, he was a Lecturer with the Naval University of Engineering. He was promoted to an Associate Professor in 2009 and to a Full Professor in 2012. He is currently the Committee Member of Department of Energy and Transportation, China Ministry of Science and Technology, Beijing, China. His current research interests include renewable energy generation, modeling and control of power electronics system and high-voltage large-capacity power electronics equipment.

**Ruitian Wang** received the B.S. degree in automation from the Huazhong University of Science and Technology, Wuhan, China, in 2008, and the M.S. and Ph.D. degrees in electrical engineering from the Naval University of Engineering, Wuhan, China, in 2010 and 2014, respectively.

In 2015, he was a Lecturer with the Naval University of Engineering, where he was promoted to an Associate Professor in 2018. His research interests include medium-voltage power electronics converter and multiobjective optimization of magnetic components.

**Shan Gao** received the B.S. and Ph.D. degrees in electrical engineering from the Huazhong University of Science and Technology, Wuhan, China, in 2008 and 2016, respectively.

He is currently a Research Assistant with the National Key Laboratory for Electromagnetic Energy, Naval University of Engineering, Wuhan, China. His research interests within power electronics include electric motor drives, microgrid, and power electronic applications.

**Jilong Liu** was born in Hebei province, China, in 1988. He received the B.S. and Ph.D. degrees in electrical engineering from the School of Electrical Engineering, Xi'an Jiaotong University, Xi'an, China, in 2010 and 2015, respectively.

From 2015 to 2017, he was a Lecturer with the National Key Laboratory of Electromagnetic Energy, Naval University of Engineering, Wuhan, China, where he was promoted to an Associate Professor in 2017, and to a Full Professor in 2022. His current research interests include modular multilevel converter and ac motor control.

**Weiwei Zhang** was born in Hubei province, China, in 1989. He received the B.S. degree in information countermeasures technology from the Nanjing University of Science and Technology, Nanjing, China, in 2012, the M.S degree in control science and engineering from the College of Logistics Engineering, Chongqing, China, in 2015, and the Ph.D. degree in electrical engineering from the Naval University of Engineering, Wuhan, China, in 2019.

He is currently working with the National Key Laboratory of Electromagnetic Energy, Naval University of Engineering. His research interests include large capacity power conversion and electric vehicle drives.